

Dark soliton states of Bose-Einstein condensates in anisotropic traps

D. L. Feder,^{1,2} M. S. Pindzola,³ L. A. Collins,⁴ B. I. Schneider,⁵ and C. W. Clark²

¹*Clarendon Laboratory, University of Oxford, Parks Road, Oxford OX1 3PU, U.K.*

²*Electron and Optical Physics Division, National Institute of Standards and Technology, Gaithersburg, MD 20899-8410*

³*Department of Physics, Auburn University, Auburn, AL 36849*

⁴*Theoretical Division, Mail Stop B212, Los Alamos National Laboratory, Los Alamos, NM 87545*

⁵*Physics Division, National Science Foundation, Arlington, Virginia 22230*

(February 1, 2008)

Dark soliton states of Bose-Einstein condensates in harmonic traps are studied both analytically and computationally by the direct solution of the Gross-Pitaevskii equation in three dimensions. The ground and self-consistent excited states are found numerically by relaxation in imaginary time. The energy of a stationary soliton in a harmonic trap is shown to be independent of density and geometry for large numbers of atoms. Large amplitude field modulation at a frequency resonant with the energy of a dark soliton is found to give rise to a state with multiple vortices. The Bogoliubov excitation spectrum of the soliton state contains complex frequencies, which disappear for sufficiently small numbers of atoms or large transverse confinement. The relationship between these complex modes and the snake instability is investigated numerically by propagation in real time.

03.75.Fi, 05.45.Yv, 42.50.-p

I. INTRODUCTION

Numerous experimental studies have confirmed the general validity of the time-dependent Gross-Pitaevskii (GP) equation [1,2] used to calculate the ground state and excitations of various Bose-Einstein condensates of trapped alkali atoms [3–5]. To map the spectrum of collective (or particle-hole) excitations, mean-field linear response theories based on the Bogoliubov approximation [6,7] or its finite temperature extensions [8,9] have been developed and applied to numerous experimental configurations.

The collective excitations are physically distinct from *self-consistent* excited states of the trapped gas. In the latter case, the stationary condensate wavefunction itself may contain one or more nodes. Indeed, the nonlinear GP equation supports many well-known self-consistent excitations, such as vortex states [10–14], and configurations with bright and dark solitons [15–19] for attractive as well as repulsive Bose gases. These contrast quite strongly with the collective excitations, which are obtained from the linear response of the condensate to an external perturbation.

In the case of a fundamental dark (or black) soliton, the condensate density vanishes along a nodal surface and the soliton velocity is zero. Such a solution is equivalent to two condensates with a phase difference of π between them, separated by a thin impenetrable barrier, and is an idealization of the nodal structures obtained recently in a two-component system [20]. Dark optical solitons in nonlinear dielectric fibers have been actively studied [21] since their prediction [22] and experimental observation [23–25]; the recent observation of solitons in trapped Bose gases [26,27] has provided another striking manifestation of nonlinear atom optics [28].

The stability of stationary dark solitons (also known as

standing waves or kinks) in trapped condensates has been the subject of recent investigations [19]. These states are thermodynamically unstable, since their energies are always higher than the nodeless self-consistent ground state. In addition, they can be dynamically unstable; in more than one dimension, an extended dark soliton in an optical fiber will generally undergo a ‘snake deformation’, where transverse modulations cause the nodal plane to decay into vortices [21]. The Bogoliubov excitation spectrum for a kink is known to contain modes with imaginary frequencies and quasiparticle amplitudes localized in the notch [19]; however, the origin of these imaginary eigenvalues and their explicit connection to a dynamical snake instability remain unclear.

In the present work, the properties and stability of self-consistent excited states of trapped Bose condensates are explored further. After a brief description in Sec. II of the formalism and techniques employed in the numerical calculations, the number-dependence of the energy of stationary dark solitons is obtained and discussed in Sec. III. In the Thomas-Fermi (TF) limit, corresponding to large condensates, the energy difference between the kink and nodeless ground states is found to be independent of the number of atoms. In order to better understand this result, the soliton energy is calculated perturbatively around the TF limit using a boundary-layer approach in Sec. IV A. It is shown that the energy of the soliton state in the TF limit is identical to that of the ‘anomalous mode’ in the Bogoliubov spectrum. Perturbation theory in the weakly interacting limit, carried out in Sec. IV B, demonstrates that this result is particular to large condensates, however. This perturbative approach also yields significant insight into the criteria for the existence of Bogoliubov excitations with complex frequencies, discussed in Sec. IV C. The relationship between complex modes and dynamical instability of the kink is

explored in Sec. V. In Sec. VI, we explore the possibility of transferring the condensate into a kink state by a field excitation. The results are summarized in Sec. VII.

II. THEORETICAL BACKGROUND

At zero temperature, the dynamics of a single-component condensate are governed by the three-dimensional (3D) time-dependent GP equation:

$$i\frac{\partial\psi(\mathbf{r},t)}{\partial t} = \left(-\frac{1}{2}\nabla^2 + V_{\text{trap}}(\mathbf{r}) + V_H(\mathbf{r},t)\right)\psi(\mathbf{r},t), \quad (1)$$

where the confining harmonic potential

$$V_{\text{trap}}(\mathbf{r}) = \frac{1}{2}(x^2 + \alpha^2 y^2 + \beta^2 z^2) \quad (2)$$

is completely anisotropic in general; in recent experiments on solitons in a Bose condensate [27], the relevant parameters were $\alpha \equiv \omega_y/\omega_x = \sqrt{2}$ and $\beta \equiv \omega_z/\omega_x = 2$. The Hartree (mean-field) potential is written

$$V_H(\mathbf{r},t) = 4\pi\eta_0|\psi(\mathbf{r},t)|^2; \quad (3)$$

choosing the condensate wavefunction $\psi(\mathbf{r},t)$ to be normalized to unity yields the strength parameter $\eta_0 = aN_0/d_x$, where a is the atomic scattering length and N_0 is the total number of atoms. We assume a condensate composed of Na atoms, in which case $a = 52a_B \approx 2.75$ nm in Bohr radii a_B [29]. The above three equations are written in reduced units, where the length scale is $d_x = \sqrt{\hbar/M\omega_x}$, the time scale is $T = 2\pi/\omega_x$, and the energy is given in units of $\hbar\omega_x$, where ω_x is the angular trap frequency in the x direction and M is the atomic mass of Na.

The ground and self-consistent excited states of Bose-Einstein condensates are obtained by direct solution of the GP equation in imaginary time ($\tau = it$). At each imaginary time step, the chemical potential $\mu \equiv \langle H \rangle / N_0$ (where H is the GP operator on the right side of Eq. (1)) is readjusted in order to preserve the norm of the wavefunction. Self-consistent excitations may be found numerically by relaxation of the GP equation toward equilibrium, subject either to special initial conditions (spatial variations of phase or amplitude [13,30]) or applied constraints (such as orthogonality to the ground state).

The initial wavefunction for the imaginary time propagation is a Gaussian $\psi(\mathbf{r},0) = f(\mathbf{r}) \exp\{-\frac{1}{2}(x^2 + \alpha^2 y^2 + \beta^2 z^2)\}$ for small numbers of atoms $N_0 \lesssim 10^5$. For larger N_0 the kinetic energy contribution to the total energy becomes negligible, and the initial state is chosen to be proportional to the Thomas-Fermi (TF) expression $f(\mathbf{r})\sqrt{(\mu_{\text{TF}} - V_{\text{trap}})/4\pi\eta_0}\Theta(\mu_{\text{TF}} - V_{\text{trap}})$. The TF chemical potential is $\mu_{\text{TF}} = \frac{1}{2}(15\alpha\beta\eta_0)^{2/5}$ in units of $\hbar\omega_x$ and $\Theta(x)$ is unity when x is positive and zero otherwise. The choice of initial state has no influence on the final result,

but can improve the time required for numerical convergence. All stationary states without circulation can be classified by their reflection symmetry in the \hat{x} , \hat{y} , and \hat{z} directions. For convenience, wavefunctions that are odd under a reflection in one spatial direction $\alpha = x, y, z$ are labelled p_α and are referred to as ‘p-wave’. Similarly, the ‘d-wave’ states $d_{\alpha\beta}$, with $\alpha, \beta = x, y, z$, have odd reflection symmetry in two directions α and β . In order to obtain p-wave or d-wave states, one may choose $f(\mathbf{r}) \propto x, y, z$ or $f(\mathbf{r}) \propto xy, xz, yz$, respectively. Since the nonlinear Hamiltonian (1) commutes with the parity operators, however, perhaps the simplest strategy is to block diagonalize the GP operator according to parity in each direction, and solve for the lowest energy state in each of the eight parity manifolds. For higher lying stationary configurations, the solution must be explicitly orthogonalized to lower-energy states during the imaginary time propagation.

We propagate the 3D time-dependent GP equation using three distinct techniques: a variable step-size Runge-Kutta (RK) method [31], second-order differencing (SOD) [32], and real-space product formula (RSPF) [33]. In the SOD and RK methods, the time propagation results from one or at most a few matrix-vector multiplies of the Hamiltonian onto a previously computed vector. The RSPF employs a split-operator approach which partitions the action of the kinetic energy matrix into a succession of 2×2 matrix operations on a known vector. It should be noted that all of these time propagators are efficiently implemented on distributed-memory massively parallel computers.

The treatment of the kinetic energy operator forms the main difference in the implementation of the propagation techniques. The SOD and RSPF methods discretize the kinetic energy operator using the simplest three-point, central finite difference (FD) formula for the second derivative operator. In the RK method, the spatial wavefunction is expanded in a discrete variable representation (DVR) [34,35] based on Gauss-Hermite quadrature. The DVR has the advantage, shared also by the FD method, that the matrix elements of all local operators are diagonal and equal to their value on the spatial grid. The DVR kinetic energy operator is dense in each dimension compared with the FD approach; however, it also provides a much more accurate representation of the derivatives than does the simple FD approximation. All of the methods scale formally with the number of spatial grid points, although the prefactor is different for each. Grids of the order of 200^3 points are used in the SOD and RSPF, while the DVR approach employs approximately 100 functions in each spatial direction.

III. STATIONARY STATES

Using the diffusion form of Eq. (1) for the condensate wavefunction, the GP equation relaxes to the stationary

state of interest. The chemical potential μ and free energy per particle $E \equiv \mu - \frac{1}{2}\langle V_H \rangle / N_0$ may be obtained as a function of the number of atoms, and the results are summarized in Tables I and II. The values of the chemical potential for the ground state agree to three significant figures with those reported earlier [35]. The probability densities in the $z = 0$ plane for p_x and d_{xy} dark soliton condensates with $N_0 = 2^{10} = 1024$ are shown in Fig. 1. The line nodes, which are clearly visible as depressions in the condensate density, widen near the surface as the condensate density decreases and the healing length diverges.

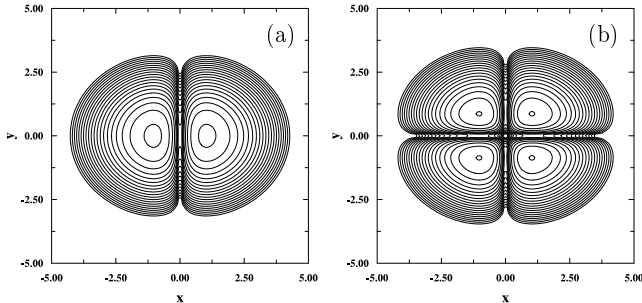


FIG. 1. The probability densities in the $z = 0$ plane for (a) p_x and (b) d_{xy} dark soliton states with $N = 2^{10} = 1024$ are shown as 2D contour maps, where radial distances are in scaled trap units d_x . Trap parameters are $\omega_x = (2\pi)177$ rad/s, $\alpha = \sqrt{2}$, and $\beta = 2$.

If the GP equation is relaxed subject to orthogonality constraints with previous solutions, many additional stationary states may be found. The first s-wave excited state, with $f(\mathbf{r}) = 1$ and constrained to be orthogonal to the ground state, has an ellipsoidal nodal surface centered about zero. The excited state with $f(\mathbf{r}) = 2x^2 - 1$ and constrained to be orthogonal to the ground state, has two nodal surfaces which intersect the x axis.

The numerical calculations indicate that the average energy per particle for a black soliton is independent of both geometry and particle number in the TF limit; this is in contrast with the energy per particle of an isolated vortex in a cylindrical trap, for example, which varies as $\Delta E_v \sim (5/2R^2)\ln(R/\xi)$ where $R = (15\eta_0)^{1/5}$ and $\xi \sim 1/R$ are respectively the mean TF radius and the healing length in units of d_x [12]. For large N_0 , the energy differences (both in the chemical potential and free energy) between the p_x and ground states converge to a constant value of approximately 0.7 in units of $\hbar\omega_x$. The energy differences of the p_y and p_z states are simply scaled by α and β , respectively; i.e. the soliton energy is $\Delta E_s \approx 0.7$ in units of $\hbar\omega_y$ and $\hbar\omega_z$. Similarly, the energies of the $d_{\alpha\beta}$ states are approximately $\Delta E_s \approx 0.7(\alpha + \beta)$.

The energy of the black soliton relative to the ground state is close to the energy $\hbar\omega/\sqrt{2}$ of the ‘anomalous mode’ in the Bogoliubov spectrum of a one-dimensional p-wave state in the TF limit [19]. This excitation has

positive energy but negative norm (or vice versa), and has been associated with the oscillation of a dark soliton in the trapped condensate at frequency $\omega/\sqrt{2}$ [18,27]. In nonlinear systems, however, there is no direct relationship between the energy differences among self-consistent states and the collective excitations from these states; for example, the precession frequency (or anomalous mode) for an isolated vortex in a cylindrical TF condensate is not $\Delta E_v/\hbar$, but rather $\frac{3}{5}\Delta E_v/\hbar$ [12]. Indeed, as shown below, the energy of a black soliton displaced from the trap center is always smaller than $\hbar\omega/\sqrt{2}$.

IV. PERTURBATIVE ANALYSIS

A. Thomas-Fermi limit

The soliton energy may be calculated using a boundary layer correction to the TF wavefunction [18,36]. The p_x state requires a plane of nodes at $x_0 = 0$, but in principle x_0 can take any value since an oscillating dark soliton becomes black at its classical turning point [18,27]. The condensate density will have the TF form everywhere except in a small region near x_0 , where the kinetic energy drives the wavefunction to zero.

In order to define a suitable perturbation parameter, it is convenient to further rescale the static GP equation (1), where the left side becomes $\tilde{\mu}\psi(\tilde{r})$, as follows: $\{x, y, z\} = R\{\tilde{x}, \tilde{y}/\alpha, \tilde{z}/\beta\}$, $\tilde{\mu} = \mu/\hbar\omega_x = R^2/2$, $\tilde{\eta}_0 = \eta_0\alpha\beta/R^5$, and $\psi^2 = \tilde{\psi}^2\alpha\beta/R^3$. Now, the normalization of the wavefunction takes the form $4\pi\tilde{\eta}_0 = \int d^3\tilde{r}\tilde{\psi}^2$. For a condensate in the TF limit with a soliton normal to the x -axis, one may neglect the kinetic energy contributions except in the x -direction. The rescaled GP equation then effectively has cylindrical symmetry:

$$\left[-\frac{\epsilon}{2} \frac{\partial^2}{\partial x^2} + \frac{1}{2} \tilde{r}^2 + \tilde{\psi}^2 - \frac{1}{2} \right] \tilde{\psi} = 0, \quad (4)$$

where $\epsilon = R^{-4}$ is small in the TF limit, and $\tilde{r}^2 = \tilde{x}^2 + \tilde{y}^2 + \tilde{z}^2 = \tilde{x}^2 + \tilde{\rho}^2$.

In the outer (slowly-varying) region, one expands $\tilde{\psi}_{\text{out}} = \chi_0 + \epsilon\chi_1 + \dots$. The TF result is recovered to zeroth order in ϵ : $\chi_0 = \pm\sqrt{(1 - \tilde{r}^2)/2}$. Of course, this solution is inconsistent with the boundary condition $\tilde{\psi}(\tilde{x} = \tilde{x}_0) = 0$, implying the existence of a boundary layer near $\tilde{x} \sim \tilde{x}_0$. In this region, the outer solution is asymptotically $\chi_0 \sim \pm\sqrt{(1 - \tilde{\rho}^2 - \tilde{x}_0^2)/2}$.

For the inner region it is preferable to define $\tilde{x} \equiv \tilde{x}_0 + \delta X$, where the boundary-layer thickness is $\delta \ll 1$ and $|X| \gg 0$ are the regions where the inner and outer solutions must match. Since the asymptotic behavior of the outer solution is known, the inner wavefunction may be expanded as $\tilde{\psi}_{\text{in}} = \pm\sqrt{(1 - \tilde{\rho}^2 - \tilde{x}_0^2)/2} [\Phi_0 + \delta\Phi_1 + \dots]$. To lowest order in δ , Eq. (4) becomes:

$$\left[\frac{\epsilon}{\delta^2} \frac{\partial^2}{\partial X^2} + (1 - \tilde{\rho}^2 - \tilde{x}_0^2) (1 - \Phi_0^2) \right] \Phi_0 = 0. \quad (5)$$

The ‘distinguished limit’ giving a nontrivial solution corresponds to $\delta = \sqrt{\epsilon} = R^{-2}$. When $|X| \gg 0$, $\Phi_0 \sim 1$ giving a perfect asymptotic match. With the substitution $X = Z/\sqrt{\frac{1}{2}(1 - \tilde{\rho}^2 - \tilde{x}_0^2)}$, Eq. (5) becomes the well-known equation for a dark soliton in the continuum $-\frac{1}{2}\frac{d^2}{dZ^2}\Phi_0 + \Phi_0^3 - \Phi_0 = 0$, yielding the exact solution for the inner wavefunction $\Phi(X) = \tanh\left[X\sqrt{\frac{1}{2}(1 - \tilde{\rho}^2 - \tilde{x}_0^2)}\right]$.

The uniform solution for the wavefunction over all space may be written as $\tilde{\psi}_{\text{unif}} = \tilde{\psi}_{\text{out}} + \tilde{\psi}_{\text{in}} - \tilde{\psi}_{\text{over}}$, where $\tilde{\psi}_{\text{over}}$ is the solution in the overlap region $|X| \gg 0$:

$$\tilde{\psi}_{\text{unif}}(\tilde{\rho}, \tilde{x}_{\lessgtr}) = \mp \sqrt{\frac{1 - \tilde{\rho}^2 - \tilde{x}^2}{2}} + \sqrt{\frac{1 - \tilde{\rho}^2 - \tilde{x}_0^2}{2}} \times \left\{ \tanh\left[\sqrt{\frac{1 - \tilde{\rho}^2 - \tilde{x}_0^2}{2}} R^2(\tilde{x} - \tilde{x}_0)\right] \pm 1 \right\}, \quad (6)$$

where the $\tilde{x}_{<}$ and $\tilde{x}_{>}$ correspond to $\tilde{x} < \tilde{x}_0$ and $\tilde{x} > \tilde{x}_0$, respectively. In principle, the chemical potential may now be found directly from the normalization condition $4\pi\tilde{\eta}_0 = \int d^3\tilde{r}\tilde{\psi}_{\text{unif}}^2$. In practice, however, the large number of cross terms resulting from squaring Eq. (6) makes this unnecessarily complicated. Rather, the integral over \tilde{x} is split into three regions: (I) $-\sqrt{1 - \tilde{\rho}^2} \leq \tilde{x} \leq \tilde{x}_a$ ($\tilde{x}_a < \tilde{x}_0$), (II) $\tilde{x}_a \leq \tilde{x} \leq \tilde{x}_b$ ($\tilde{x}_b > \tilde{x}_0$) or $X_a \leq X \leq X_b$ ($X_a \rightarrow -\infty$ and $X_b \rightarrow \infty$), and (III) $\tilde{x}_b \leq \tilde{x} \leq \sqrt{1 - \tilde{\rho}^2}$. Since the inner and outer solutions are asymptotically equal in the overlap regions, the result cannot depend on the particular choices of \tilde{x}_a and \tilde{x}_b . One readily obtains:

$$\tilde{\eta}_0 = \frac{\alpha\beta\eta_0}{R^5} = \frac{1}{15} - \frac{\sqrt{2}}{6R^2}(1 - \tilde{x}_0^2)^{3/2}, \quad (7)$$

which may be inverted to yield the chemical potential for the soliton state

$$\begin{aligned} \tilde{\mu}_s &= \frac{\mu_s}{\hbar\omega_x} = \frac{1}{2}(15\alpha\beta\eta_0)^{2/5} + \frac{1}{\sqrt{2}}(1 - \tilde{x}_0^2)^{3/2} \\ &= \tilde{\mu}_{\text{TF}} + \frac{1}{\sqrt{2}}(1 - \tilde{x}_0^2)^{3/2}. \end{aligned} \quad (8)$$

The correction to the chemical potential in the TF limit is $1/\sqrt{2}$ when the soliton is at the origin $\tilde{x}_0 = 0$, corresponding to the p-wave state, and is zero when the soliton is at the surface of the cloud $\tilde{x}_0 = 1$. Since $\mu = \partial E/\partial N$, the energy per particle for the soliton is

$$\frac{E_s}{N_0} = \frac{5}{7}\mu_{\text{TF}} + \frac{1}{\sqrt{2}}(1 - \tilde{x}_0^2)^{3/2}\hbar\omega_x.$$

The corrections for $\tilde{x}_0 = 0$ agree with the numerical values, and are independent of both geometry and number at this level of approximation. Physically, the dark soliton has a constant energy as the number of atoms increases, because its area increases as R^2 while its width diminishes as $\xi^2 \sim 1/R^2$ [12]. A similar invariant is used as a measure of soliton stability in optical fibers [37]. As

the transverse soliton confinement becomes more appreciable (i.e. by increasing the frequencies ω_y and ω_z), however, the kinetic energy in this direction will grow, and the low-order boundary-layer result will lose its validity.

Two views of a black soliton state defined by Eq. (6) are shown in Fig. 2. In the first, the density with a soliton displaced from the origin, $x_0 = 3d_x$, is shown along the x -axis, and is compared with the TF ground state solution. The condensate containing a notch soliton bulges slightly overall in order to conserve the total number of atoms; the radii for the TF and soliton states are $d_x\sqrt{2\tilde{\mu}_{\text{TF}}}$ and $d_x\sqrt{2\tilde{\mu}_s}$, respectively. In the second view, the soliton state is shown as a density plot in the xy -plane. The boundary layer theory to lowest order captures the divergence of the healing length in the vicinity of the cloud surface. In actuality, a displaced soliton would most likely be curved in order for the nodal plane to intersect the cloud boundary at a surface normal; such curvature is found for travelling dark solitons [27] and for displaced vortices in rotating trapped condensates [13,14].

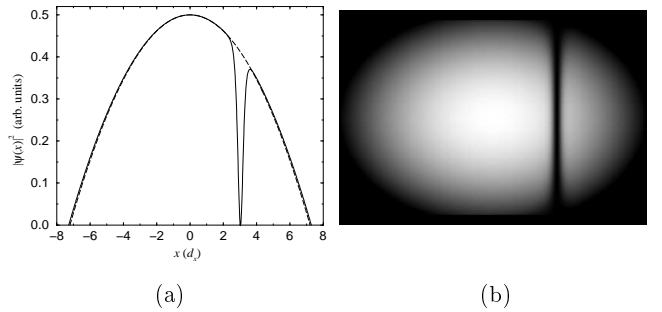


FIG. 2. The boundary-layer approximation (6) for a condensate containing a soliton at $x_0 = 3d_x$ is shown for $N_0 = 2^{18} = 262,144$ atoms, $\omega_x = (2\pi)177$ rad/s, $\alpha = \sqrt{2}$, and $\beta = 2$. In (a), the view is along the x -axis; the solid and dashed lines correspond to the soliton and TF ground states, respectively. In (b), the soliton state is depicted as a density plot in the xy -plane.

B. Low density limit: Energy differences and anomalous mode

The boundary layer analysis indicates that the energy of the self-consistent p_x state in the TF limit is exactly equal to the frequency of the anomalous mode in the Bogoliubov spectrum. In order to determine whether this holds for all densities, it is useful to consider the opposite limit of small condensates where analytical results can be easily obtained.

The perturbation expansion for the time-independent GP equation (1) requires expanding the condensate wavefunction $\psi = \psi_0 + \lambda\psi_1$ and chemical potential $\tilde{\mu} = \tilde{\mu}_0 + \lambda\tilde{\mu}_1$ in powers of $\lambda \equiv 4\pi\eta_0$. The normalized unperturbed p_x state is

$$\psi_0 = \left(\frac{4\alpha\beta}{\pi^3}\right)^{1/4} x e^{-(x^2 + \alpha y^2 + \beta z^2)/2} \quad (9)$$

and $\tilde{\mu}_0 = \frac{1}{2}(3 + \alpha + \beta)$. Making use of the readily derived expression for a purely real condensate wavefunction

$$\tilde{\mu}_1 = \int d^3r \psi_0^4 = \frac{3}{8\pi} \sqrt{\frac{\alpha\beta}{2\pi}}, \quad (10)$$

one immediately obtains the first order correction to the chemical potential

$$\mu \approx \left(\tilde{\mu}_0 + \frac{3}{2} \sqrt{\frac{\alpha\beta}{2\pi}} \eta_0 \right) \hbar\omega_x. \quad (11)$$

The low-lying excitations ε may be obtained using the Bogoliubov equations

$$\begin{aligned} \left(-\frac{1}{2}\nabla^2 + V_{\text{trap}} + 2V_H - \tilde{\mu} \right) u - V_H v &= \tilde{\varepsilon} u \\ \left(-\frac{1}{2}\nabla^2 + V_{\text{trap}} + 2V_H - \tilde{\mu} \right) v - V_H u &= -\tilde{\varepsilon} v, \end{aligned} \quad (12)$$

where $u = u(\mathbf{r})$ and $v = v(\mathbf{r})$. These equations may be written in the more convenient form $(H_0 + \lambda H_1) \psi = \tilde{\varepsilon} \Psi$, where

$$\begin{aligned} H_0 &= \begin{pmatrix} -\frac{1}{2}\nabla^2 + V_{\text{trap}} - \tilde{\mu}_0 & 0 \\ 0 & \frac{1}{2}\nabla^2 - V_{\text{trap}} + \tilde{\mu}_0 \end{pmatrix}, \\ H_1 &= \begin{pmatrix} 2\psi_0^2 - \tilde{\mu}_1 & \psi_0^2 \\ -\psi_0^2 & \tilde{\mu}_1 - 2\psi_0^2 \end{pmatrix}, \quad \Psi = \begin{pmatrix} u \\ v \end{pmatrix}. \end{aligned} \quad (13)$$

For arbitrary trap anisotropy, there are always two degenerate modes with energy $\tilde{\varepsilon} = \varepsilon/\hbar\omega_x = 1$ in the unperturbed p_x state; these are the dipole and anomalous modes with positive and negative unit norms, respectively:

$$\Psi_1 = \begin{pmatrix} 1 \\ 0 \end{pmatrix} \left(\frac{\alpha\beta}{4\pi^3} \right)^{1/4} (2x^2 - 1) e^{-(x^2 + \alpha y^2 + \beta z^2)/2}, \quad (14)$$

$$\Psi_2 = \begin{pmatrix} 0 \\ 1 \end{pmatrix} \left(\frac{\alpha\beta}{\pi^3} \right)^{1/4} e^{-(x^2 + \alpha y^2 + \beta z^2)/2}. \quad (15)$$

Note that the ‘ground state’ is the p-wave condensate wavefunction given in Eq. (9). The degeneracy between these states is lifted by the perturbing Hamiltonian H_1 , and the first-order corrections to the eigenvalues follow directly from the diagonalization of the resulting non-symmetric $g \times g$ matrix

$$\langle \Psi_i | H_1 | \Psi_j \rangle, \quad i, j = 1, 2, \dots, g, \quad (16)$$

where g is the degeneracy. Direct application of Eq. (16) with $g = 2$ yields no finite-number correction for the dipole mode, as expected, while the energy of the anomalous mode becomes

$$\varepsilon_a \approx \left(1 - \frac{1}{4} \sqrt{\frac{\alpha\beta}{2\pi}} \eta_0 \right) \hbar\omega_x. \quad (17)$$

Evidently, the value of the anomalous mode in the p_x state is not generally equal to the difference (10) in the chemical potentials between the p-wave and s-wave states

$$\Delta\mu = \left(1 + \frac{3}{2} \sqrt{\frac{\alpha\beta}{2\pi}} \eta_0 \right) \hbar\omega_x. \quad (18)$$

Indeed, the perturbative corrections do not even have the same sign.

C. Low density limit: Complex modes

It is instructive to consider the special case where all of the trapping frequencies are equal, $\alpha = \beta = 1$. In this geometry, according to Ref. [19], an infinitesimal condensate number gives rise to pure imaginary frequencies. Assuming a p_x state, one may define $\rho^2 \equiv y^2 + z^2$ and block diagonalize the Hamiltonian into states of definite angular momentum $L_x = m\hbar$. In the $m = 0$ manifold, in addition to the dipole (14) and anomalous (15) excitations, there is a third mode with $\tilde{\varepsilon} = 1$:

$$\Psi_3 = \begin{pmatrix} 1 \\ 0 \end{pmatrix} \frac{1}{\pi^{3/4}} (1 - \rho^2) e^{-(x^2 + \rho^2)/2}. \quad (19)$$

Diagonalizing the resulting 3×3 matrix (16), one again obtains no correction for the dipole mode. The remaining degenerate modes, however, split into complex conjugate pairs with energies

$$\varepsilon = \left[1 - \frac{1}{8\sqrt{2\pi}} (3 \pm i\sqrt{7}) \eta_0 \right] \hbar\omega_x. \quad (20)$$

These results are compared with numerical calculations for a spherical trap in Fig. 3. The numerics are extremely close to the expression (20) for small η_0 , but show deviations by $\eta_0 \sim 0.1$.

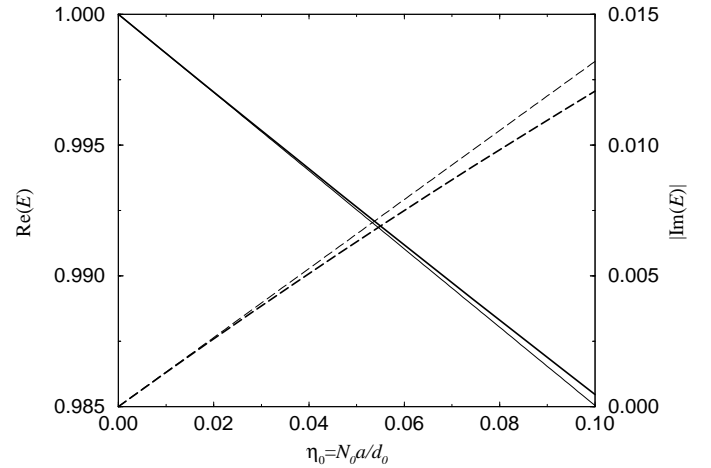


FIG. 3. The real (solid lines) and imaginary (dashed lines) part of the complex excitation frequencies for $m = 0$ are shown as a function of $\eta_0 = N_0 a / d_0$ for a spherical trap. Light and dark lines correspond to analytical (20) and numerical calculations, respectively.

The corresponding complex eigenvectors both have zero norm $\int d^3r (|u_i|^2 - |v_i|^2) \equiv \int d^3r \Psi_i^* \sigma_3 \Psi_i = 0$, and satisfy the boundary conditions $u, v \rightarrow 0$ as $\mathbf{r} \rightarrow \infty$:

$$\Psi'_2 = \Psi_1 - \sqrt{2}\Psi_2 - \frac{\sqrt{2}}{4} (1 - i\sqrt{7}) \Psi_3; \quad (21)$$

$$\Psi'_3 = \Psi_1 - \sqrt{2}\Psi_2 - \frac{\sqrt{2}}{4} (1 + i\sqrt{7}) \Psi_3. \quad (22)$$

The condensate coupling between the axial and radial modes gives rise to modes with frequencies that are *complex*, rather than purely imaginary as assumed in [19]. It is important to note that the existence of complex Bogoliubov excitations does not violate the general condition on the quasiparticle amplitudes [7]:

$$(\varepsilon_i - \varepsilon_j^*) \int d^3r (u_j^* u_i - v_j^* v_i) = 0. \quad (23)$$

If $i = j$ and ε_i is complex, the corresponding particle-hole eigenfunction must have zero norm.

For any given number of condensate atoms N_0 in a cylindrically symmetric trap, there is a critical anisotropy $\omega_\rho/\omega_x = \alpha$ such that all the Bogoliubov excitations of the p-wave state become purely real [19]. Indeed, in the limit $N_0 \rightarrow 0$ considered here, any $\alpha > 1$ is sufficient to ensure the disappearance of the complex modes because the degeneracy between the anomalous and transverse modes is broken by the anisotropy.

For $\alpha < 1$, complex modes can arise in many m states. In this regime, there exist numerous additional unperturbed anomalous modes with energy $\tilde{\varepsilon}_{nm} = 1 - \alpha(2n + m) \geq 0$ but negative norm (since $u = 0$) that are degenerate with eigenstates having energy $\tilde{\varepsilon}_{n'm'} = \alpha(2n' + m') - 1 \equiv \tilde{\varepsilon}_{nm}$ and positive norm ($v = 0$). It is interesting to determine if the nonlinear coupling among these degenerate modes gives rise to complex excitations even in the limit of vanishing transverse confinement, $\alpha \rightarrow 0$. Consider the $m = 0$ manifold and $\alpha = 1/q$ with even integer $q \rightarrow \infty$. Degeneracies occur when the axial quantum numbers for both the u and v are zero and the radial numbers $n_u = \frac{q}{2} + p$ and $n_v = \frac{q}{2} - p$, respectively, where $0 \leq p \leq \frac{q}{2}$. When $p = \frac{q}{2}$, the unperturbed energy is $\tilde{\varepsilon}_0 = 1$, but since the terms in Eq. (16) involving $\Psi_3 \propto L_q^{(0)}/q!$ will be smaller than the other terms by a factor $1/q!$, this complex mode vanishes in the limit $q \rightarrow \infty$. In the opposite limit $p = 0$, the unperturbed energy is $\tilde{\varepsilon}_0 = 0$, and the quasiparticle amplitudes become

$$u = v = \frac{L_{q/2}^{(0)}(\rho/\sqrt{q})}{\pi^{3/4} \sqrt{q} (q/2)!} e^{-(\rho^2/q + x^2)/2} \\ \sim J_0(\sqrt{2}\rho) e^{-x^2/2}, \quad q \rightarrow \infty. \quad (24)$$

Note that this $u = v$ solution has even x -symmetry and therefore does not correspond to the Goldstone mode. The condensate wavefunction ψ in Eq. (9) becomes independent of ρ , and the 2×2 matrix (16) immediately yields the imaginary eigenvalues

$$\varepsilon = \pm i \sqrt{\frac{3\pi}{2}} n_0 a d_x^2 \hbar \omega_x, \quad (25)$$

where $n_0 = N_0/\mathcal{V}$ is the condensate density in the system volume \mathcal{V} . The same solution is found for all values of m in this limit. Thus, even in the absence of transverse confinement, the excitation spectrum of the p_x state contains complex modes, in agreement with the results of Ref. [19].

Additional insight into the limit of transverse deconfinement may be gained by assuming translational invariance in \hat{x} and \hat{y} at the outset. With the axial quantum numbers zero, the unperturbed energies for the u and v become $\tilde{\varepsilon}_0^u = \frac{1}{2} (k_y^u{}^2 + k_z^u{}^2) - 1$ and $\tilde{\varepsilon}_0^v = 1 - \frac{1}{2} (k_y^v{}^2 + k_z^v{}^2)$. When these are degenerate, the off-diagonal couplings are non-zero only if $k_y^u = k_y^v = k_y$ and $k_z^u = k_z^v = k_z$, enforcing the condition $\tilde{\varepsilon}_0^u = \tilde{\varepsilon}_0^v = 0$ and $k_y^2 + k_z^2 = k^2 = 2$. Note that the unperturbed energy $\varepsilon_0 = 0$ and relevant wavevector $|k| = \sqrt{2}$ are the same as in the infinitely weak trap limit considered above. The perturbing matrix (16) consists of an infinite number of identical 2×2 submatrices for a given value of k_x and $k_y = \sqrt{2 - k_x^2}$. Each submatrix corresponds to a different value of m in the cylindrical case considered above, and yields the imaginary modes

$$\varepsilon_k = \pm i \sqrt{\frac{3\pi}{2}} n_0 a d_x^2 \frac{\hbar^2 k^2}{2M} = \pm i \sqrt{\frac{3\pi}{2}} n_0 a d_x^2 \hbar \omega_x, \quad (26)$$

in agreement with the result (25).

Summarizing the results of this section, in the limit of weak particle interactions or low condensate densities, we have found that the anomalous mode frequency does not correspond to the frequency difference between the excited and ground state energies. In addition, solitons are unstable in a sufficiently loose trap. For solitons oriented in the radial direction of a cylindrically symmetric trap, imaginary eigenvalues appear in the Bogoliubov excitation spectrum when the axial frequency begins to exceed the radial frequency. These modes persist in the limit of vanishing radial confinement.

V. COMPLEX EXCITATIONS AND SNAKE INSTABILITY

The explicit connection between the existence of excitations with complex frequencies and the dynamic instability of the p-wave state remains unclear. This ‘snake instability’ is well known in the nonlinear optical community [21], and is associated with the undulation of the nodal plane in the radial direction. It has been conjectured that the complex modes are responsible for the snake instability [19]; however, these modes have zero norm by definition (23), so it is not clear how they can become occupied. It is important, therefore, to determine if the wavelength of the undulation matches the spatial dependence of complex modes in the Bogoliubov

spectrum, and if the snake instability disappears when the excitation frequencies become purely real.

The low-lying complex modes for a stationary p-wave condensate are determined numerically using the Bogoliubov equations (12). For ease of computation, the trap is assumed to be cylindrically symmetric, $\rho^2 = y^2 + z^2$, with the condensate wavefunction odd under reflection in axial direction \hat{x} . In Fig. 4 are shown the complex modes in the excitation spectrum as a function of radial confinement, for a trap with axial frequency $\omega_x = 2\pi \cdot 50$ rad/s containing a condensate with 10^4 atoms. All complex modes have even axial parity. For relatively weak trap anisotropy $\omega_\rho/\omega_x \equiv \alpha \lesssim 3$, there are several complex modes with angular momentum projections $m = 0, 1, 2$. As α increases, these modes disappear in turn until only one purely imaginary mode with $m = 1$ remains. Its magnitude reaches a maximum at $\alpha \approx 6$, and vanishes at $\alpha \approx 10$. A similar removal of the imaginary modes can be effected by decreasing the particle number at fixed geometry.

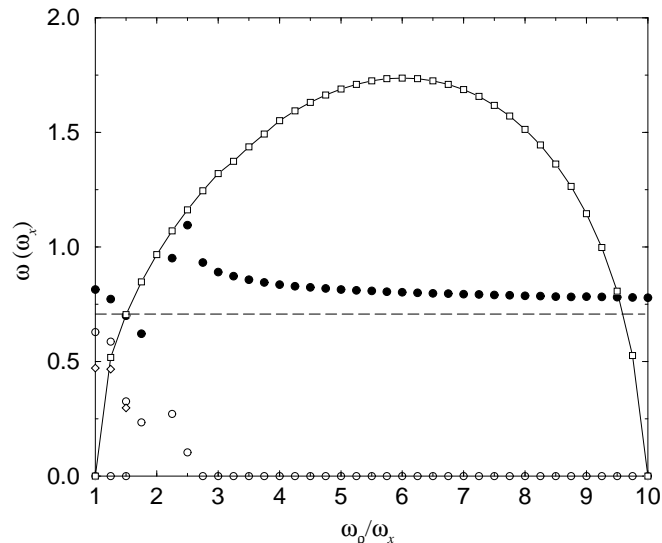


FIG. 4. The real (filled symbols) and imaginary (open symbols) parts of the low-lying complex excitation frequencies are given as a function of the trap anisotropy $\alpha \equiv \omega_\rho/\omega_x$ for a cylindrically symmetric trap, where the condensate is in a p_x state with 10^4 atoms and $\omega_x = 2\pi \cdot 50$ rad/s. Excitations with $m = 0, 1$, and 2 are represented by circles, squares, and diamonds, respectively; the dashed line denotes the TF estimate of the anomalous mode.

For large anisotropy $\alpha \gg 1$, the stability criterion is expected to be approximately $\alpha_c \geq \tilde{\mu}/2.4$ [19], where $\tilde{\mu} = \mu/\hbar\omega_x$. In the TF approximation, $\alpha_c \geq 7.6$ for the geometry considered above. The larger value required here is due to deviations from the TF limit; the radial wavefunction approaches a Gaussian when the transverse confinement is strong. When $\alpha = 10$, the TF chemical potential is $\mu_{\text{TF}} = 23.88\hbar\omega_x$ while the actual value is

determined to be $\mu \approx 26.89\hbar\omega_x$.

The dynamic stability of dark soliton excited states is investigated by propagation of the GP equation in *real* time for an extended period. In the absence of an applied perturbation, the self-consistent states should remain absolutely stationary. In practice, however, numerical noise inherent in the propagation algorithm is magnified by the nonlinearity. Although the norm and chemical potential are conserved to one part in 10^{12} and 10^{15} respectively during the numerical propagation, the kink state eventually decays. In order to make contact with the complex excitation frequencies in Fig. 4, we considered the cases $\alpha = 1, 6$, and 10 . For the first two cases, the modes with the largest imaginary component are $\epsilon = 0.63i\hbar\omega_x$ and $1.74i\hbar\omega_x$; the p-wave states were found to decay in real time in approximately 160 ms and 40 ms, respectively. The third case with $\alpha = 10$ remained stable for the longest propagation time considered, 200 ms. Thus, the lifetime of the p-wave state appears qualitatively to scale with the inverse of the largest imaginary mode in the excitation spectrum.

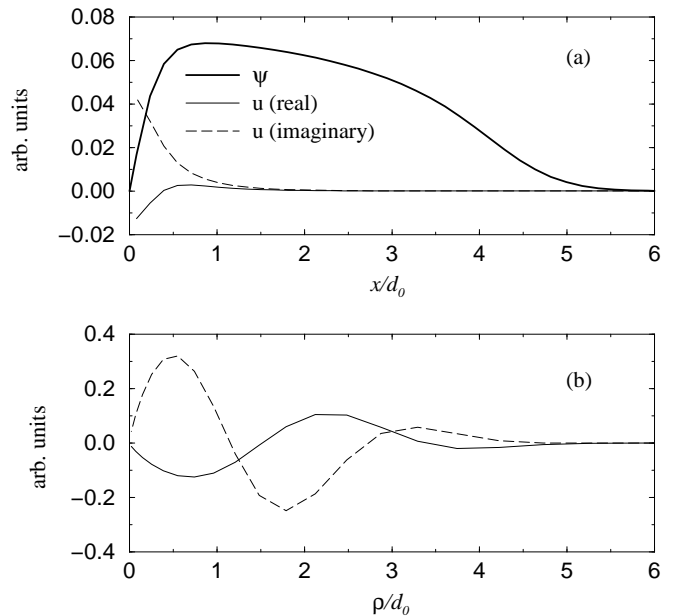


FIG. 5. The spatial variation of the mode in the Bogoliubov spectrum with the largest imaginary component $\epsilon = 2.16i\hbar\omega_x$ is shown for a p_x -wave condensate containing 10^5 atoms in a spherical trap $\omega_\rho/\omega_x = 1$ with $\omega_x = 2\pi \cdot 50$ rad/s. The axial ($\rho = 0, x > 0$) and radial ($x = 0$) dependences of the complex u amplitude are shown in (a) and (b), respectively (note that ψ and u are odd and even in x , respectively, and that $|u| = |v|$ for this pure imaginary mode). The axial dependence of the condensate wavefunction is shown for comparison in (a).

As illustrated in Figs. 5 and 6, there is a close similarity between the spatial variation of the eigenmode with the largest imaginary component and that of the soliton nodal plane during the initial decay. For a p-wave state

in a spherical trap, such as the one considered above but with 10^5 atoms, the relevant excitation is purely imaginary with an energy $\epsilon = 2.16i\hbar\omega_x$, and $|u| = |v|$ (as is the case for all pure imaginary modes). Fig. 5 shows the corresponding radial and axial dependences of the complex u Bogoliubov amplitude. The quasiparticle amplitudes are highly localized axially, but oscillate radially within the soliton nodal plane. It is interesting to note that the imaginary components of the excitation energies tend to *decrease* as the number of radial nodes increases; this behavior is due to the effective negative kinetic energy of the dark soliton [18], and is reminiscent of internal waves at the interface between layers in stratified fluid mixtures [38].

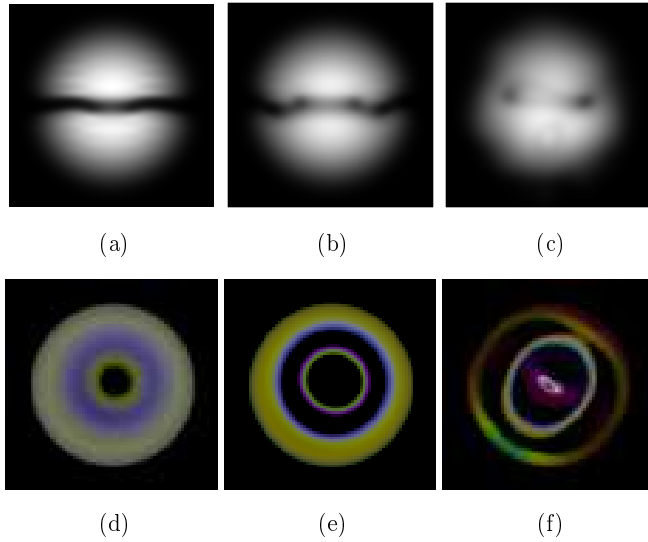


FIG. 6. Snapshots of the snake instability are shown for a p_y -wave condensate containing 10^5 atoms in a spherical trap with $\omega = 2\pi \cdot 50$ rad/s. Times after the initial formation of the soliton state are 47 ms, 50 ms, and 77 ms for (a)-(c) and (d)-(f). In (a)-(c), the brightness is proportional to the condensate density, and the images correspond to densities integrated down the line of sight. In (d)-(f), the brightness is *inversely* proportional to the condensate density, and regions outside the TF sphere are rendered transparent in order to visualize nodes in the condensate interior; the color corresponds to the phase: $\phi = 0$ through 2π is represented by the sequence red-green-blue-red. The view is perpendicular to nodal plane; prior to the snake instability the black soliton would appear as a featureless disk.

In Fig. 6, snapshots of the snake instability are shown for a p_y -wave state in a spherical trap [for convenience, the axis perpendicular to the nodal line is taken to be along \hat{y} , the vertical direction in Fig. 6(a)-(c)]. The GP equation is solved on a Cartesian mesh with no parity restrictions. After approximately 40 ms of real time propagation, the black soliton begins to undulate. The spatial variations are symmetric about the y -axis, originating near the center and propagating outwards. The over-

all shape follows closely that of the largest u amplitude shown in Fig. 5: the two radial nodes of this imaginary excitation correspond to stationary points in the soliton bending. At an intermediate time, Fig. 6(e), the soliton has decayed into two concentric vortex rings whose cores are located at these nodes. The outer vortex ring decays rapidly (by 75 ms) to the condensate surface, where it shrinks considerably, as shown in Fig. 6(f); the inner ring was found to remain stable for much longer times. The vortex rings are barely visible in the integrated densities shown in Fig. 6(a)-(c), so we expect the experimental observation of these intriguing features using standard absorption imaging to be a challenge. The decay of the soliton into vortex rings produces a large number of density oscillations, which are required in order to conserve the total energy of the system and which are undamped in the present formalism. At long times, these oscillations are most evident at the condensate surface, giving rise to the bright halo in Fig. 6(f).

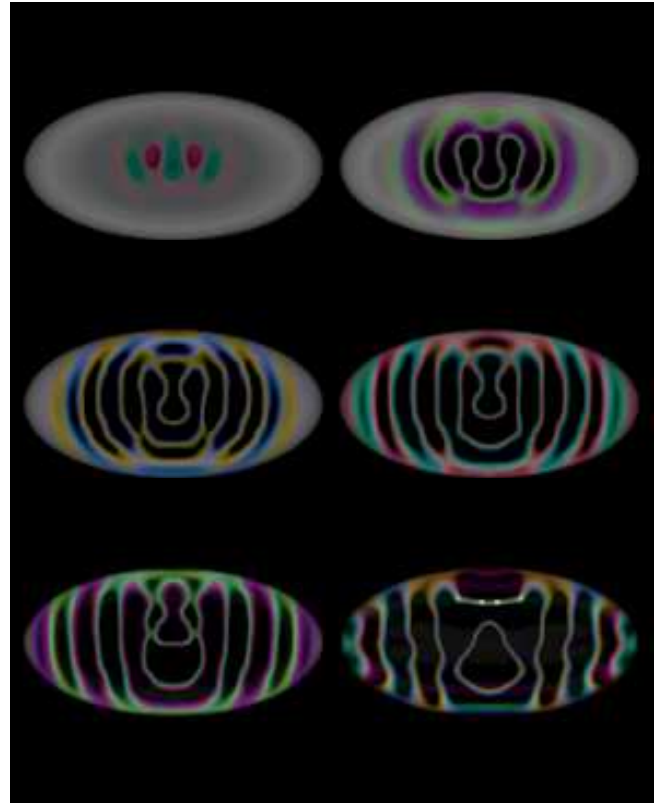


FIG. 7. The breakup of a p_y state is shown as a function of time for $N_0 = 10^6$ atoms, $\omega_x = (2\pi)14$ rad/s, $\alpha = \sqrt{2}$, and $\beta = 2$. From the top left to the bottom right in raster order are shown times $t = 15$ ms through 20 ms in 1 ms increments after the initial state is formed. The view is along \hat{y} , and the Hamiltonian was constrained to even parity along \hat{x} and \hat{z} for ease of computation. The rendering is identical to that of Figs. 6(d)-(f). The filamentation is almost entirely constrained to the original nodal xz -plane.

It is interesting to investigate the snake instability for parameters relevant to recent experiments on dark solitons in trapped condensates [27]. Fig. 7 shows the breakup of a black soliton in a completely anisotropic trap containing one million Na atoms. The undulations are already pronounced by 12 ms, and radiate outwards from the soliton center as found above. Unlike the spherically symmetric condensate shown in Fig. 6, however, the soliton does not decay into concentric vortex rings far from its center, but rather into a series of approximately evenly spaced curved vortex lines in the direction of weakest confinement (taken to be \hat{x}). The results imply that the largest imaginary mode in the Bogoliubov excitation spectrum has an energy of $\sim 6\hbar\omega_x$ and has 14 nodes along \hat{x} . At longer times, the innermost two vortex rings make contact with one another, and subsequently detach into a vortex line and a ring. The simulations indicate a rich dynamics among quantized vortices in these systems that are only beginning to be explored [39].

VI. FIELD EXCITATION

Several techniques have been proposed for the experimental production of dark solitons in trapped condensates, including adiabatic Raman transitions to the p-wave state [16], preparation of the condensate in a superposition of two internal states [17], collisions between two separate condensates [40], and phase imprinting [41]; the last approach was recently implemented experimentally [26,27]. For small particle interactions, the self-consistent excited states (such as a p-wave or d-wave condensate with at least one stationary dark soliton) approach the non-interacting single-particle excitations of the harmonic trap. In this regime, it might be possible to transfer most of the condensate into a soliton state by applying an external field resonant with the energy difference between the ground and excited self-consistent states.

We have attempted to excite the d_{xy} dark soliton state for a small condensate containing $N_0 = 1024$ atoms in a completely anisotropic trap, shown in Fig. 1(b). The field excitation is modeled by a large-amplitude time-dependent spatial perturbation in the GP equation (1) given by $V_{\text{add}}(\mathbf{r}, t) = A(t)xy \cos(\omega_p t)$, where the amplitude $A(t)$ is 25% of a trap energy $\hbar\omega_x$ and includes a smooth turn on and turn off as a function of time. The probe frequency is set at $\omega_p = 2.06$, which is the separation in chemical potential of the ground and first d_{xy} state (cf. Table II).

The time-dependent probability density in the $z = 0$ plane is shown in Fig. 8 with snapshots at $t = T_p$, $4T_p$, $7T_p$, and $10T_p$, where $T_p = 2\pi/\omega_p \approx 0.5T$. At $t = T_p$, the wavefunction overlap with the ground state is 0.98 and with the d_{xy} state is 0.01. Until $t = 4T_p$, the wavefunction overlap with the ground state decreases monotonically to 0.57, while the overlap with the d_{xy} state

increases to a maximum of 0.25. Thereafter, as illustrated at times $t = 7T_p$ and $t = 10T_p$, the wavefunction overlaps with both the ground and this particular dark soliton state decrease. While the perturbing potential is not able to yield a d_{xy} state, the last image in Fig. 8 at $t = 10T_p$ shows the formation of a number of depressions in the probability density at the very edge of the condensate, corresponding to multiple vortices with both senses of circulation.

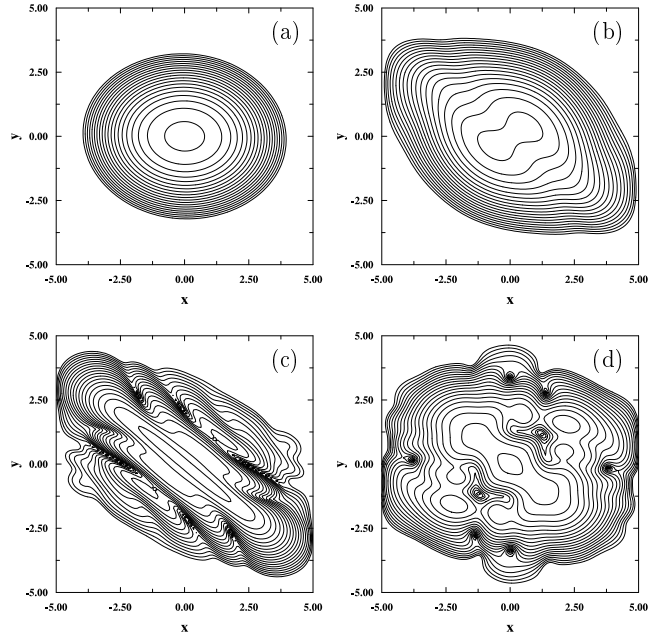


FIG. 8. The probability density in the $z = 0$ plane for the time evolution of the ground state with $N = 1024$ under a time-varying spatial perturbation is shown as a contour map at (a) $t = T_p \approx 0.5T$, (b) $t = 4T_p$, (c) $t = 7T_p$, and (d) $t = 10T_p$. Radial distances are in scaled trap units d_x , and trap parameters are $\omega_x = (2\pi)177$ rad/s, $\alpha = \sqrt{2}$, and $\beta = 2$. In (d), density minima at the top and bottom correspond to vortices, those at left and right to antivortices.

The inability of a field excitation to produce dark solitons is not surprising, in light of the snake instabilities discussed in Sec. V. Dark solitons are unstable against the formation of vortices under ideal conditions, and are increasingly unstable in the presence of an external perturbation. Nevertheless, applying a very large amplitude perturbation may be a viable alternative approach for the formation of vortices in systems with much larger condensate densities; this possibility remains for future work.

VII. CONCLUSIONS

In summary, self-consistent ground and excited states of a condensate in an anisotropic harmonic trap are calculated by direct solution of the time-dependent GP equation in three dimensions. The energy of a dark soliton at

the center of the trap, relative to the true ground state, is found to be independent of both the number of atoms and the trap geometry in the TF limit, with a value equal to the soliton oscillation frequency. In the weakly interacting limit, however, the energy of the anomalous mode does not equal the energy of the dark soliton. In both limits, the low-lying Bogoliubov excitation spectrum of p-wave states is found to contain modes with complex frequencies, which may be removed by strong trap confinement in the soliton plane or by decreasing the condensate density. These complex modes are shown to give rise to the snake instability of the solitons observed in real time propagation of the GP equation. In extended trap geometries, the solitons are found to decay into vortex lines and rings at long times, imposing constraints on the ability to generate and observe these intriguing excitations in current experimental geometries.

ACKNOWLEDGMENTS

The authors are grateful to G. M. Bruun, P. Colarusso, P. S. Julienne, W. P. Reinhardt, and J. Simsarian for stimulating discussions, and to P. Ketcham for his assistance in generating the color figures. This work was supported in part by the National Science Foundation (MSP), and by the U.S. Office of Naval Research (DLF and CWC). Part of the computational work was carried out at the National Energy Research Supercomputer Center at Lawrence Berkeley National Laboratory. Work (LAC) performed under the auspices of the U.S. Department of Energy through the Los Alamos National Laboratory.

-
- [1] E. P. Gross, *Nuovo Cimento* **20**, 454 (1961).
 - [2] L. P. Pitaevskii, *Zh. Eksp. Teor. Fiz.* **40**, 646 (1961) [*Sov. Phys. JETP* **13**, 451 (1961)].
 - [3] A. S. Parkins and D. F. Walls, *Physics Reports* **303**, 1 (1998).
 - [4] F. Dalfovo, S. Giorgini, L. P. Pitaevskii, and S. Stringari, *Rev. Mod. Phys.* **71**, 463 (1999).
 - [5] W. Ketterle, D. S. Durfee, and D. M. Stamper-Kurn, in *Bose-Einstein Condensation in Atomic Gases, Proceedings of the International School of Physics "Enrico Fermi" Course CXL*, ed. M. Inguscio, S. Stringari, and C. E. Wieman (IOS Press, Amsterdam 1999), p. 67.
 - [6] N. N. Bogoliubov, *J. Phys.* **11**, 23 (1947).
 - [7] A. L. Fetter, *Ann. Phys.* **70**, 67 (1972).
 - [8] A. Griffin, *Phys. Rev. A* **53**, 9341 (1996).
 - [9] D. A. W. Hutchinson, R. J. Dodd, and K. Burnett, *Phys. Rev. Lett.* **81**, 2198 (1998).
 - [10] R. J. Dodd, K. Burnett, M. Edwards, and C. W. Clark, *Phys. Rev. A* **56**, 587 (1997).
 - [11] D. S. Rokhsar, *Phys. Rev. Lett.* **79**, 2164 (1997); D. S. Rokhsar, e-print: cond-mat/9709212; D. A. Butts and D. S. Rokhsar, *Nature* **397**, 327 (1999).
 - [12] A. A. Svidzinsky and A. L. Fetter, *Phys. Rev. A* **58**, 3168 (1998); A. A. Svidzinsky and A. L. Fetter, e-print: cond-mat/9811348; A. L. Fetter, in *Bose-Einstein Condensation in Atomic Gases, Proceedings of the International School of Physics "Enrico Fermi" Course CXL*, ed. M. Inguscio, S. Stringari, and C. E. Wieman (IOS Press, Amsterdam 1999), p. 201.
 - [13] D. L. Feder, B. I. Schneider, and C. W. Clark, *Phys. Rev. Lett.* **82**, 4956 (1999); D. L. Feder, B. I. Schneider, and C. W. Clark, *Phys. Rev. A* **61**, 011601 (2000).
 - [14] Y. Castin and R. Dum, *Eur. Phys. Jour. D* **7**, 399 (1999).
 - [15] W. P. Reinhardt and C. W. Clark, *J. Phys. B* **30**, L785 (1997).
 - [16] R. Dum, J. I. Cirac, M. Lewenstein, and P. Zoller, *Phys. Rev. Lett.* **80**, 2972 (1998).
 - [17] O. Zobay, S. Pötting, P. Meystre, and E. M. Wright, *Phys. Rev. A* **59**, 643 (1999).
 - [18] Th. Busch and J. Anglin, *Phys. Rev. Lett.* **84**, 2298 (2000).
 - [19] A. E. Muryshev, H. B. van Linden van den Heuvell, and G. V. Shlyapnikov, *Phys. Rev. A* **60**, R2665 (1999); P. O. Fedichev, A. E. Muryshev, and G. V. Shlyapnikov, *Phys. Rev. A* **60**, 3220 (1999).
 - [20] M.R. Matthews *et al.*, *Phys. Rev. Lett.* **83**, 2498 (1999).
 - [21] Yu. S. Kivshar and B. Luther-Davies, *Phys. Rep.* **298**, 81 (1998).
 - [22] A. Hasegawa and F. Tappert, *Appl. Phys. Lett.* **23**, 142 (1973).
 - [23] Ph. Emplit *et al.*, *Opt. Commun.* **62**, 374 (1987).
 - [24] D. Krökel, N. J. Halas, G. Giuliani, and D. Grischkowsky, *Phys. Rev. Lett.* **60**, 29 (1988).
 - [25] A. M. Weiner *et al.*, *Phys. Rev. Lett.* **61**, 2445 (1988).
 - [26] S. Burger *et al.*, *Phys. Rev. Lett.* **83**, 5198 (1999).
 - [27] J. Denschlag *et al.*, *Science* **287**, 97 (2000).
 - [28] L. Deng *et al.*, *Nature* **398**, 218 (1999).
 - [29] P. S. Julienne, F. H. Mies, E. Tiesinga, and C. J. Williams, *Phys. Rev. Lett.* **78**, 1880 (1997).
 - [30] C. Huepe, S. Metens, G. Dewel, P. Borckmans, and M. E. Brachet, *Phys. Rev. Lett.* **82**, 1616 (1999).
 - [31] *Numerical Recipes in C, Second Edition*, ed. W. H. Press, S. A. Teukolsky, W. T. Vetterling, and B. P. Flannery (Cambridge University Press, Cambridge, 1992).
 - [32] C. Leforestier *et al.*, *J. Comp. Phys.* **94**, 57 (1991).
 - [33] H. De Raedt, *Comp. Phys. Rep.* **7**, 1 (1987); L. Collins, J. Kress, and R. Walker, *Comp. Phys. Comm.* **114**, 15 (1998).
 - [34] J. C. Light, I. P. Hamilton, and J. V. Lill, *J. Chem. Phys.* **82**, 1400 (1985).
 - [35] B. I. Schneider and D. L. Feder, *Phys. Rev. A* **59**, 2232 (1999).
 - [36] A. L. Fetter and D. L. Feder, *Phys. Rev. A* **58**, 3185 (1998).
 - [37] W. J. Tomlinson *et al.*, *J. Opt. Soc. Am. B* **6**, 329 (1989).
 - [38] J. Lighthill, *Waves in Fluids* (Cambridge University Press, Cambridge, 1978).
 - [39] B. M. Caradoc-Davies, R. J. Ballagh, and P. B. Blaikie, e-print: cond-mat/0003063.

- [40] T. F. Scott, R. J. Ballagh, and K. Burnett, J. Phys. B **31**, L329 (1998).
[41] L. Dobrek *et al.*, Phys. Rev. A **60**, R3381 (1999).

TABLE I. The chemical potential μ and free energy per particle E of the ground state (subscript 0) and p-wave dark solitons oriented along x , y , and z are given as a function of the number of atoms in the condensate N_0 in units of $\hbar\omega_x$.

N_0	μ_0	E_0	μ_x	E_x	μ_y	E_y	μ_z	E_z
2^{10}	3.57	2.99	4.40	3.87	4.79	4.27	5.36	4.85
2^{12}	5.42	4.20	6.20	5.02	6.56	5.40	7.09	5.95
2^{14}	8.90	6.59	9.64	7.36	9.98	7.71	10.47	8.23
2^{16}	15.13	10.96	15.85	11.70	16.17	12.03	16.63	12.52
2^{18}	26.10	18.75	26.80	19.47	27.12	19.79	27.57	20.25
2^{20}	45.28	32.41	45.94	33.10	46.28	33.43	46.72	33.88

TABLE II. The chemical potential μ and free energy per particle E of the ground state (subscript 0) and d-wave dark solitons with nodes along (x, y) , (x, z) , and (y, z) are given as a function of the number of atoms in the condensate N_0 in units of $\hbar\omega_x$.

N_0	μ_0	E_0	$\mu_{x,y}$	$E_{x,y}$	$\mu_{x,z}$	$E_{x,z}$	$\mu_{y,z}$	$E_{y,z}$
2^{10}	3.57	2.99	5.63	5.16	6.20	5.74	6.60	6.15
2^{12}	5.42	4.20	7.33	6.22	7.87	6.77	8.23	7.16
2^{14}	8.90	6.59	10.72	8.48	11.21	9.00	11.55	9.35
2^{16}	15.13	10.96	16.89	12.77	17.35	13.26	17.67	13.59
2^{18}	26.10	18.75	27.83	20.51	28.27	20.97	28.59	21.29
2^{20}	45.28	32.41	46.94	34.12	47.38	34.57	47.73	34.90